



Experimental study on melt and flow characteristics and pore structure of iron ore



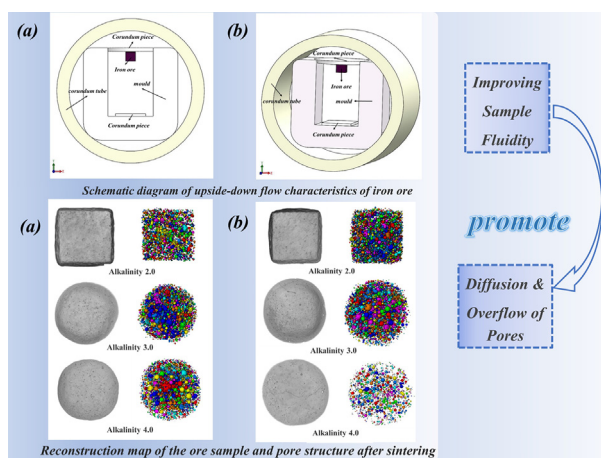
Mengting Ji, Jiawei Luo, Hao Zhou*

State Key Laboratory of Clean Energy Utilization, Institute for Thermal Power Engineering, Zhejiang University, Hangzhou, 310027, PR China

HIGHLIGHTS

- Temperature, alkalinity and ore type decide the melt and flow characteristics.
- The liquid-phase fluidity of mixed iron ore behaved best.
- Visual upside-down measurement method can fully assess the flow characteristic.
- Improving sample fluidity promotes the pores' diffusion, break and overflow.

GRAPHICAL ABSTRACT



ARTICLE INFO

Article history:

Received 26 April 2022

Received in revised form 21 September 2022

Accepted 2 October 2022

Available online 8 October 2022

Keywords:

Iron ore sintering
Visual measurement method
Melt characteristic
Flow characteristic
Evolution of pore structure

ABSTRACT

The liquid phase formed during the sintering of iron ore greatly influences the quality of the sintered ore. This paper aims to study the melt and flow characteristics of iron ore and analyze the variation law of pore structure with fluidity of iron ore during sintering. First, the melt characteristic and liquid phase flow index of five iron ores and their mixtures were investigated, with the mixed ores performing best. A method for measuring the flow characteristic was developed to study mixed iron ores with different alkalinity. This measurement method allowed the simultaneous acquisition of flow velocity, characteristic temperature and bottom curvature to comprehensively assess the flow characteristic. Finally, the effect of the flow characteristic on the pore structure and distribution of sintered ores was investigated by X-ray computed tomography. The results showed that improving the fluidity of the sintered ores would promote the diffusion and overflow of pores.

© 2022 Elsevier Ltd. All rights reserved.

1. Introduction

Iron ore sintering is an indispensable part of the iron and steel metallurgy industry. Before blast furnace ironmaking, the iron ore

feedstock must be sintered to prepare a sintered ore with excellent properties (Yang et al., 2022).

The melt and flow characteristics of iron ore at high temperatures are critical indicators to measure the sintering performance of ore. The ore with better melting performance is easier to form the liquid phase in the sintering process. In general, a sintered material with good fluidity has a wide range of effective binding

* Corresponding author.

E-mail address: zhouhao@zju.edu.cn (H. Zhou).

and the surrounding mixed sintered material is more likely to agglomerate. If the fluidity of the liquid phase is too high, an excessively molten sintered layer will form and the sintered layer will become less permeable. In addition, the excess liquid phase can also lead to the thinning of the bonding layer of the nearby mixture and the appearance of a thin-walled macro-porous structure, which reduces the structural strength of the sinter and affects its reduction (Zhang et al., 2020).

For the melt and flow characteristics of ore, many scholars (Dong et al., 2015; Liu et al., 2014; Ma et al., 2020; Peng et al., 2017; Wu et al., 2014, 2019; Wu and Zhai, 2018; Xiao et al., 2017; Zhai et al., 2020) evaluated the samples' flow characteristic by changing the vertical projection area of iron ore before and after sintering. Some scholars (Ni et al., 2020; Wu et al., 2017; Zhai et al., 2020; Zhou et al., 2015b) also evaluated the degree of reaction between the original melt and iron ore by placing the 15 wt% CaO and Fe₂O₃ chemical reagent on the pressed iron ore sheet. Kou et al. (Kou et al., 2019) used a charge coupled device (CCD) camera to study various iron ores' softening and melting processes, and the obtained ore melting curve defined some characteristic temperatures. Kasai and others (Kasai et al., 2000) suspended the ore sample in the furnace and used a precision electronic scale to detect the temperature of the first drop of the melt.

The liquid phase flow characteristic of iron ore directly impacts the pore structure. If the ore has a poor melt characteristic, it is difficult to form a liquid phase. As a result, the internal porosity of the sintered ore is quite high and such sintered ores are usually of low strength (Ni et al., 2020). The traditional method of studying pores by optical microscope can only observe and count the pore structure in two dimensions but cannot comprehensively observe the pore distribution, size and evolution under different conditions. The mercury intrusion method cannot ascertain the distribution state, and the connection form of the pores in the internal space of the sinter is impossible to ascertain (Wang et al., 2020). X-ray computed tomography (XCT) technology can overcome the above shortcomings. Through XCT, the sintered model can be reconstructed non-destructively, and the distribution of pores can be effectively observed (Shatokha et al., 2010; Zhou et al., 2021b, 2017; Zhou et al., 2020b).

In summary, the ore's flow characteristic and pore structure directly affect the quality of the sinter. The liquid flow characteristic measurement method can only obtain a single measurement result. This paper develops a visual method for measuring the flow characteristic. The method can simultaneously use parameters such as flow velocity, characteristic temperature, and bottom curvature to evaluate the flow characteristic of the ore comprehensively. In this work, the melt characteristic and liquid phase flow index of iron ores of different alkalinity were first investigated, and their performance was evaluated. The results showed that mixed iron ore had the best fluidity. The flow characteristic of mixed iron ores with different alkalinity was then measured using the developed method of flow characteristic. Finally, XCT results elucidated the effect of the high-temperature flow characteristic of iron ores on pore evolution.

Table 1
Size distribution and density of sintering raw materials (wt.%).

	Cumulative mass% passing (size in mm, dry basis)										Bulk density (kg/m ³)
	8	6.3	3.2	1.18	0.6	0.3	0.15	0.106	0.075	0.063	
Ore A (Australia)	81.1	75.3	56.2	35.3	23.9	14	7	4.7	3.2	2.4	1908.10
Ore B (Australia)	95.9	91.1	70.8	51.4	42	32.2	21	15.3	10.5	7.6	2183.90
Ore C (Australia)	95.8	87.9	64	44.4	35.9	27.4	16.8	11.8	8	5.9	2204.90
Ore D (Brazil)	92.6	87.6	68	51.9	45.4	39.8	31.8	25.8	20.1	15.6	2281.70
Ore E (Brazil)	90.8	87.5	73.7	56.1	43.8	29.1	18.5	15	12.9	9.6	2270.00

2. Experimental

2.1. Raw material preparation

The raw materials used are five kinds of iron ores and quicklime. Table 1 shows different iron ores' size distribution and bulk density (Zhou et al., 2020a). The five iron ores used in this study came from Australia and Brazil and had a wide size distribution ranging from 0 to 10 mm. Table 2 shows the chemical composition of each raw material. The iron ore samples were dried in an oven at 105 °C and then crushed using a grinding mill. The grinder crusher could entirely crush samples with a particle size of up to 26 mm. Then, the crushed iron ore was sieved with a vibrating sifter and a sieve, and particles >250 μm were re-crushed until the iron ore samples were thoroughly sieved.

The mixed iron ore composition is given in Table 3. The ore ratios used in this experiment are those commonly used in the Asian region.

By changing the mass fraction of quicklime reagent, iron ore raw materials with binary alkalinity of 2.0, 3.0, and 4.0 (Ore-2.0, Ore-3.0, and Ore-4.0) (Zhang et al., 2014b) were obtained. The ingredient list of the samples is shown in Table 4. 5 g of iron ore raw materials with different alkalinities were mixed thoroughly, and the samples were pressed at 130 MPa into a cube with a cross-sectional area of 15 mm × 15 mm.

2.2. Experimental equipment and methods

The experiment of the melt characteristic: The binary alkalinity of iron ore used was designed to be 4.0. The experimental setup is shown in Fig. 1. The corundum tube had a diameter of 100 mm and a length of 1000 mm, and the corundum piece had a diameter of 50 mm. The homemade mullite mold was a semi-cylindrical shape of 1000 mm diameter with a circular slot of 50 mm diameter in the middle, just large enough to hold the corundum piece. The thermocouple was positioned a little above the center of the corundum tube. The iron ore samples were placed on corundum pieces and pushed into the furnace for sintering. The temperature was raised from room temperature to 1050 °C in an air atmosphere at a heating rate of 10 °C/min and then heated at a rate of 5 °C/min until the iron ore melted. The CCD camera was used to capture the image of the iron ore's melt process.

The melt characteristic of the corresponding samples was judged by the area and height change rate of the iron ore samples. The edge contour was extracted from the original 24-bit image captured by the CCD camera using the self-written program of MATLAB software. As shown in Fig. 2, the height and area of the corresponding sample could be calculated by distinguishing the distribution of pixels in the contour area. The height change rate β_H and the area change rate β_A are as follows:

$$\beta_H = H/H_0 \quad (1)$$

$$\beta_A = A/A_0 \quad (2)$$

Table 2
Chemical components of each raw material (wt.%) (Zhou et al., 2015a; Zhou et al., 2021b).

Raw material	TFe	Al ₂ O ₃	SiO ₂	MgO	CaO	P	S	LOI1000
Ore A (Australia)	58.07	1.26	5.09	0.07	0.08	0.04	0.02	10.20
Ore B (Australia)	62.39	2.23	4.28	0.13	0.15	0.08	0.02	3.51
Ore C (Australia)	60.62	2.25	4.45	0.08	0.05	0.07	0.03	5.91
Ore D (Brazil)	64.31	0.79	5.42	0.17	0.09	0.01	0.03	1.09
Ore E (Brazil)	64.98	1.26	2.36	0.07	0.06	0.02	0.01	2.03
Quicklime	0.18	0.57	0.61	4.48	93.98	0	0	0

Table 3
Mixed iron ore composition (Zhou et al., 2022; Zhou et al., 2019).

Iron ore	Mixing ratio (wt.%)
Ore A (Australia)	33.33
Ore B (Australia)	16.67
Ore C (Australia)	16.67
Ore D (Brazil)	16.67
Ore E (Brazil)	16.67

Table 4
Mass ratio of samples with different alkalinity.

The ratio of iron ore to quicklime (iron ore (wt.%) / quicklime (wt.%))			
Binary alkalinity (CaO/SiO ₂)	2.0	3.0	4.0
Ore A	90.2/9.8	85.8/14.2	81.8/18.2
Ore B	91.7/8.3	87.9/12.1	84.4/15.6
Ore C	91.3/8.7	87.4/12.6	83.8/16.2
Ore D	89.6/10.4	85.1/14.9	80.9/19.1
Ore E	95.2/4.8	92.9/7.1	90.7/9.3
Mixed Ore	91.3/8.7	87.4/12.6	83.8/16.2

Where H_0 and A_0 respectively represent the initial value of the height and area of the sample; H and A respectively represent the height and area of the sample at a certain moment.

Liquid phase flow index experiment: Iron ore samples with different alkalinity were heated in a specific way in a tube furnace. The temperature changes in an actual iron ore sinter bed could not be fully simulated due to the limited heating rate of the tube furnace, which could not reach the heating rate of the actual sintering process. The corundum tube had a higher temperature in the middle than at the ends, so rapid heating and cooling of the sample could be achieved by changing the position of the sample. The center of furnace temperature was heated to 1300 °C or 1320 °C, and

the locations corresponding to the 600 °C and 1000 °C temperatures were calibrated with the S-type thermocouple. During the heating process, the iron ore sample was first kept at a position corresponding to 600 °C for 4 min, then at a position corresponding to 1000 °C for 2 min and finally at the target temperature for 4 min. During the cooling process, the samples were pushed to positions corresponding to 1000 °C and 600 °C and held for 2 min, respectively, then the samples were removed and cooled naturally. The above method could compensate to a certain extent for the lack of heating speed of the equipment. The vertical projected area of the sintered iron ore samples on the corundum piece was calculated by Image J software. The liquid phase flow index was calculated according to the following formula.

$$\text{Liquid phase flow index} = (\text{Area after flow}) / (\text{Initial area}) - 1 \quad (3)$$

Flow Characteristic Experiment: An innovative upside-down flow characteristic measurement method was adopted, and its operation procedure and subsequent data processing of the experiment have been elaborated in our previous work (Luo et al., 2021). The experimental schematic is shown in Fig. 3. As the temperature increased, the bottom of the sample continued to move closer to the generated liquid phase, and the bottom gradually tended to bend under surface tension. The morphological change model is shown in Fig. 4. Among them, L (mm), v (mm/min), and K (mm⁻¹) represents the total length of the sample, the flow velocity, and the curvature of the bottom of the sample, respectively.

Pore image processing: To explore the pore structure of mixed iron ores with different alkalinity after sintering at 1300 °C and 1320 °C, XCT was used to scan the images of the samples after sintering. In this case, the samples were sintered at 1300 °C and 1320 °C in the same way as the liquid phase flow index experiment described above. The XCT scanning voltage and current were 190.0 kV and 450.0 μA, respectively, the exposure time was set

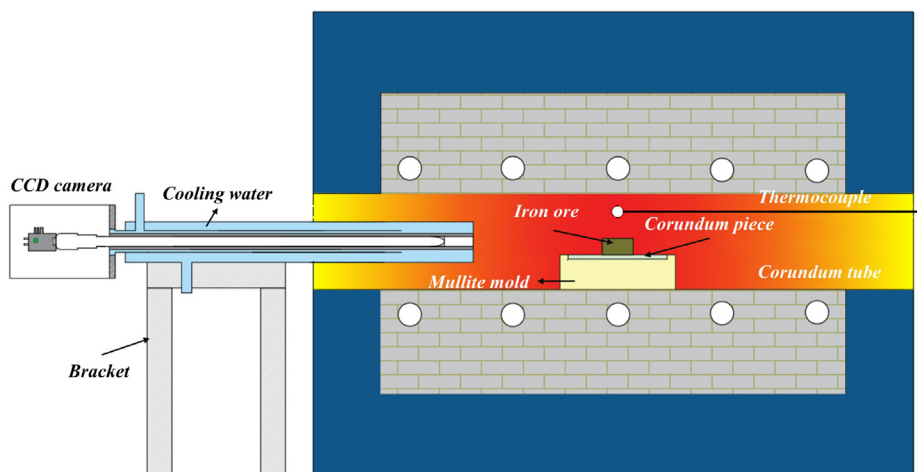


Fig. 1. Schematic diagram of the test setup for the melt characteristic and liquid phase flow index.

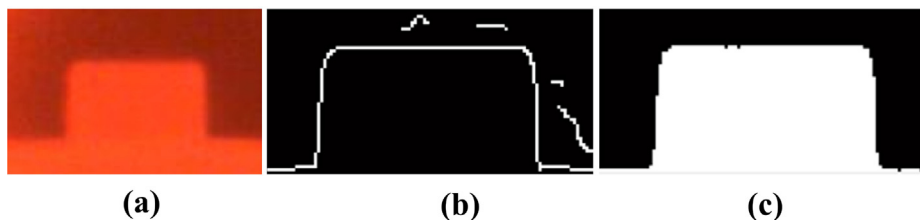


Fig. 2. Image processing process. (a) Original image; (b) Contour extraction; (c) Binary image.

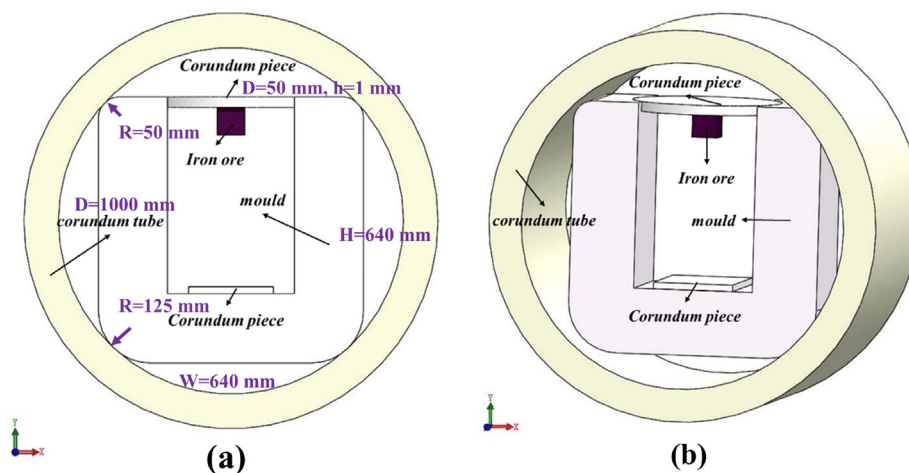


Fig. 3. Schematic diagram of the upside-down flow characteristic of iron ore.

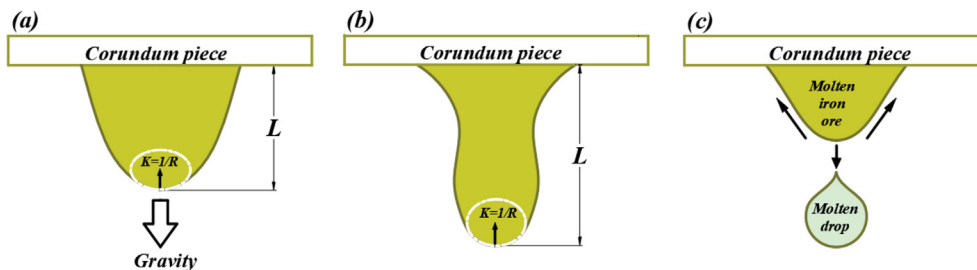


Fig. 4. Schematic diagram of the morphological changes of iron ore during the flow process.

to 0.60 s, and the scanning accuracy was 40.2 μm . The following formula can calculate the overall porosity of the iron ore sample.

$$\varphi = 1 - \frac{V_s}{V_t} \quad (4)$$

Among them, φ represents the overall porosity of the sample; V_t represents the total volume of the iron ore sample, mm^3 ; V_s represents the volume of the solid phase of the ore, mm^3 .

3. Results and discussion

3.1. Melt characteristic at variable temperature

3.1.1. Morphological change rate

Fig. 5 shows the melt characteristic of the iron ore samples as a function of temperature. In Fig. 5 (a), the morphological change of Ore A could be roughly divided into a slow decline, a rapid decline, and a melting stage. The morphological change process of Ore A with temperature is shown in Fig. 6. The rate of morphological change decreased slowly until 1275 $^{\circ}\text{C}$, which may be due to the densification of the particles during the sintering of the iron ore

(Wang et al., 2021). The rate of morphological change decreased rapidly in the range 1275–1325 $^{\circ}\text{C}$. In this temperature range, the sample produced a high liquid phase content, and the liquid phase began to flow and diffuse in all directions. As the temperature increased, the morphological change rate dropped sharply and the sample entered the melting stage. When the temperature was at about 1330 $^{\circ}\text{C}$, the height and area change rate decreased to about 20 %, and Ore A could be considered to have basically melted. The rapid morphological changes in the sample during the melting phase are caused by several factors. At sufficiently high temperatures, the iron ore sample’s liquid phase content soars, resulting in the sample softening and collapsing. Also, the fluid viscosity of the iron ore decreases with increasing temperature (He et al., 2021; Zhang et al., 2021) and the ability of the sample to flow and spread around increases (Wang et al., 2021).

The sinter melting stage of Ore B (Fig. 5(b)) was roughly similar to Ore A. Significantly, the rate of change in height and area of the samples increased slightly at about 1225 to 1260 $^{\circ}\text{C}$. This may be due to thermal expansion due to gas generation inside the iron ore or trapped air (Ilic et al., 2003). The melting curve of Ore C (Fig. 5(c)) is very different from Ore A and Ore B. When the

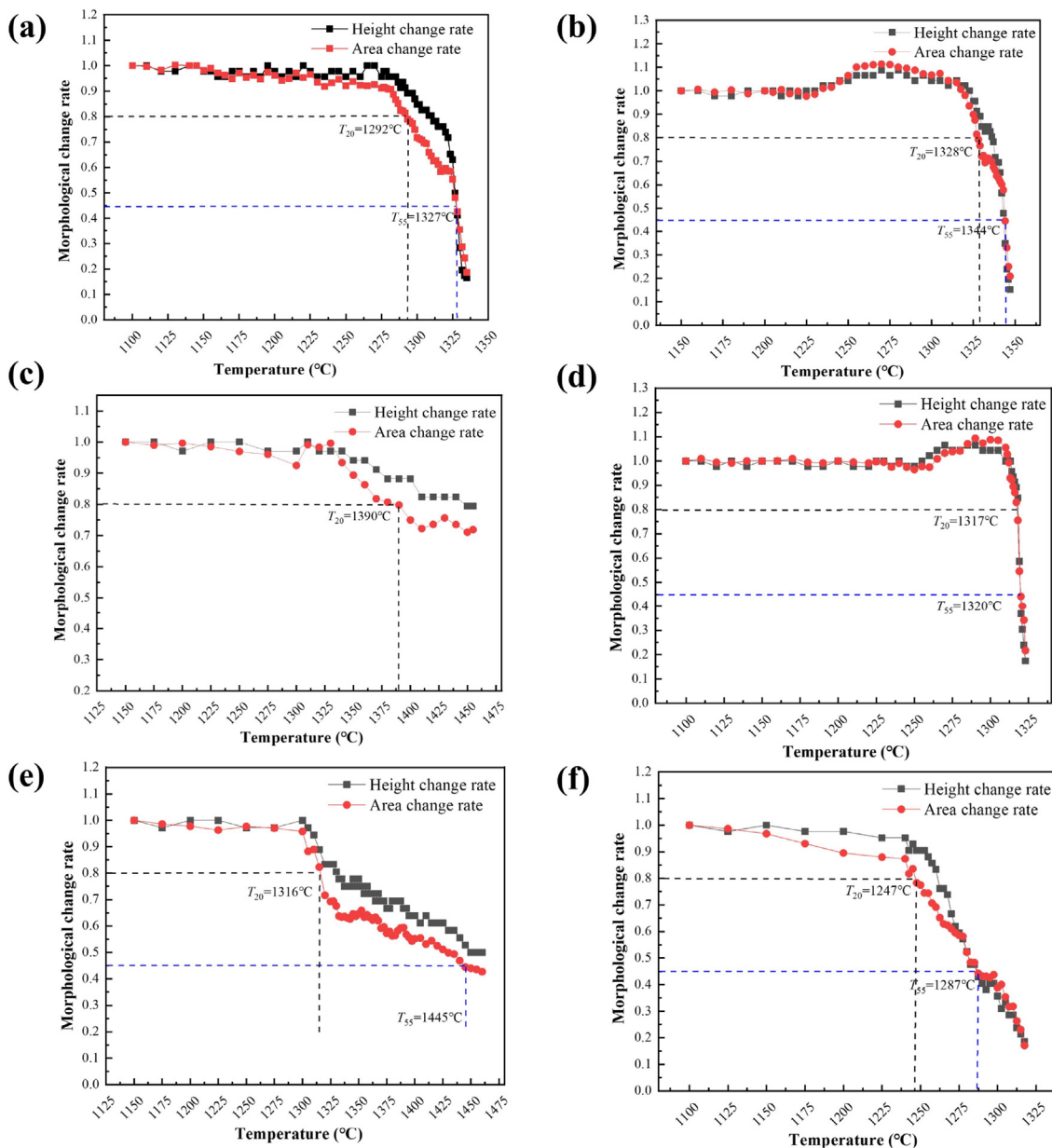


Fig. 5. Morphological change rate as a function of temperature of (a) Ore A (b) B (c) C (d)D (e)E (f) Mixed iron ore.

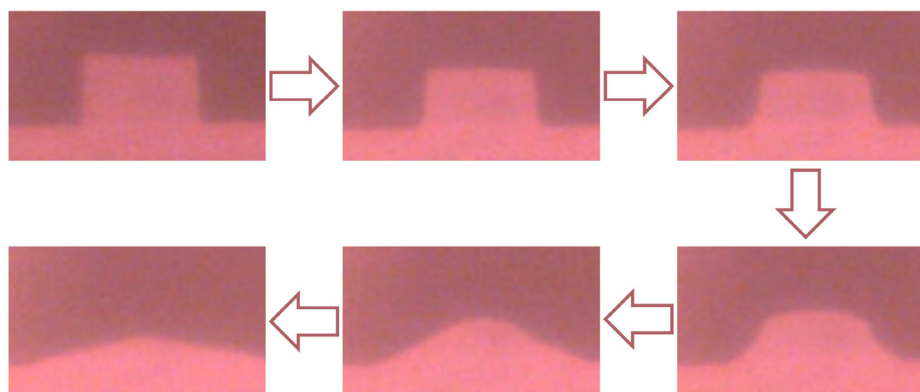


Fig. 6. Morphological change processes of Ore A during sintering.

Table 5
Melt characteristic temperature of different iron ores.

Type of ore	T_{20} (°C)	T_{55} (°C)	T_R (°C)
Ore A	1292	1327	35
Ore B	1328	1344	16
Ore C	1390	>1460	>70
Ore D	1317	1320	3
Ore E	1316	1445	129
Mixed Ore	1247	1287	40

temperature reached 1450°C, there was still no apparent melting of the whole sample and a less liquid phase. The temperature was not increased further because the actual temperature of the iron ore sintering did not reach that high. The morphological change curve

of Ore D (Fig. 5(d)) was closer to that of Ore B. The ore D also expanded to some extent within 1250 to 1290 °C. This sintered ore will be relatively more porous under the same conditions during actual sintering. Ore D was nearly completely melted by 1325 °C and the temperature range of the melting process was very narrow, which was unfavorable in the actual sintering process. Iron Ore E (Fig. 5(e)) had no noticeable morphological changes before 1300°C. When the temperature reached 1450 °C, the area and height change rates were approximately 40 % and 50 %, respectively, meaning that the sample did not melt completely. Before 1240°C, the mixed iron ore sample's height and area change rates (Fig. 5 (f)) decreased slowly, followed by a rapid decrease. The height change rate curve fluctuated slightly around 1290°C and almost entirely melted around 1320°C.

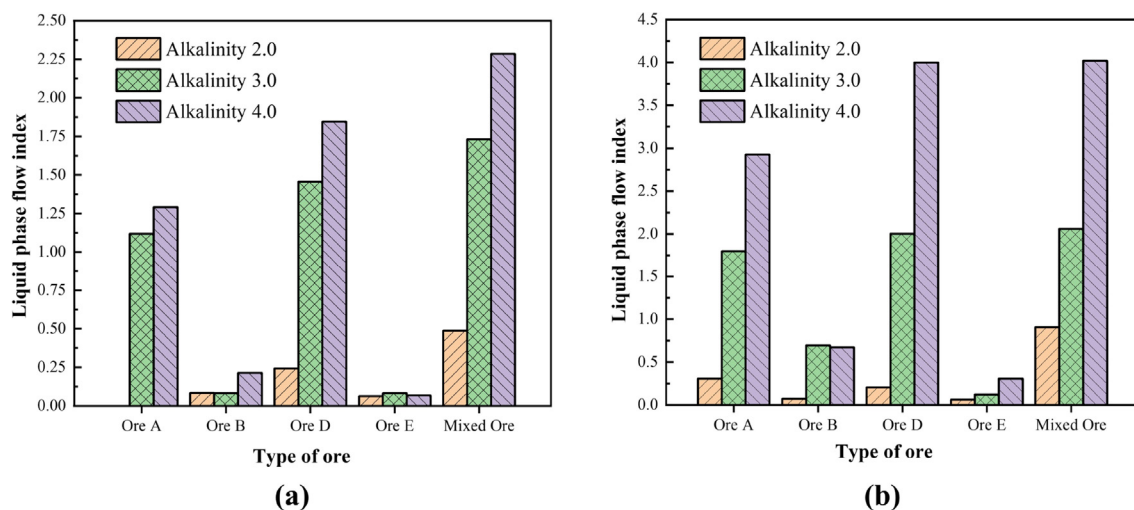


Fig. 7. Liquid phase flow index of each ore under sintering at (a) 1300 °C and (b) 1320 °C.

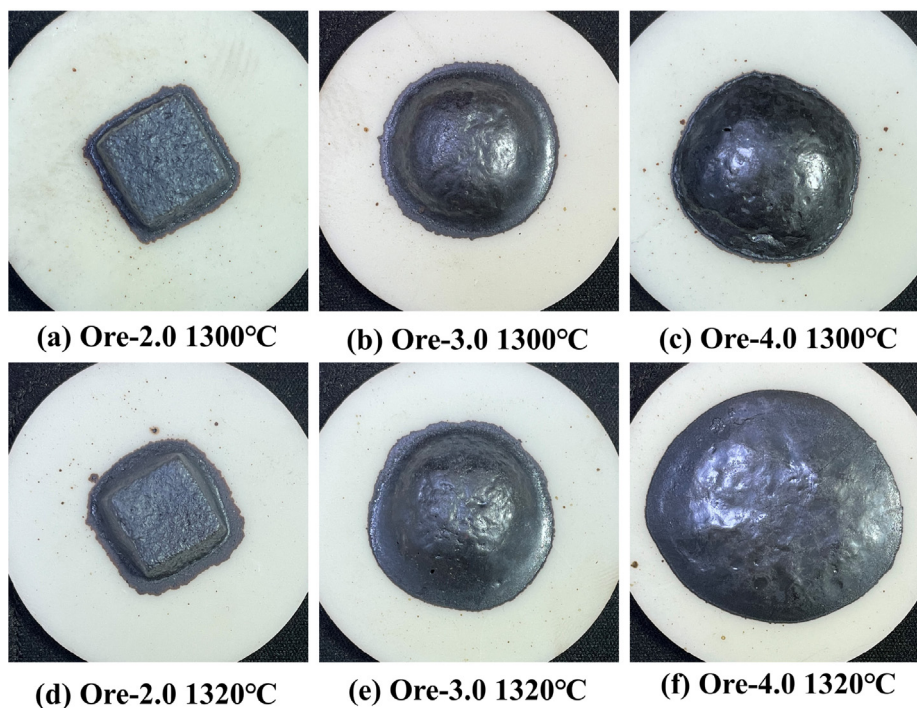


Fig. 8. Top view of sintered (a)Ore-2.0 at 1300 °C (b) Ore-3.0 at 1300 °C (c) Ore-4.0 at 1300°C (d)Ore-2.0 at 1320 °C (e) Ore-3.0 at 1320 °C (f) Ore-4.0 at 1320 °C.

In Summary, if the height and area change of the sample was reduced to 0.2 as a criterion for sample melting, the melt characteristics of the iron ore from strong to weak would be Mixed Ore > Ore D > Ore A > Ore B > Ore E > Ore C.

3.1.2. Melt characteristic temperature

In practical applications, the melt characteristic of iron ore should not be too poor. To further evaluate the iron ore's melt characteristic, referring to the practice of Kou et al. (Kou et al., 2019), three melt characteristic parameters were defined: T_{20} , T_{55} , and T_R . T_{20} and T_{55} represent the corresponding temperatures when the area change rate of the sample decreases by 20 % and 55 %, respectively. T_{20} reflects the initial temperature of the effective liquid phase, and T_{55} is the over-melting temperature of iron ore or the termination temperature of the effective liquid phase. T_R is defined as the difference between T_{55} and T_{20} , i.e., $T_R = T_{55} - T_{20}$, reflecting the controllable range of sintering temperature. The lower the sensitivity of iron ore to the change of sintering temperature, the greater the value of T_R .

Table 5 summarizes the experimental results of the melt characteristic temperatures of the iron ores mentioned above. The T_{20} and T_{55} of the mixed iron ores are relatively the lowest. The T_{20}

of Ore C is as high as 1390°C, and its T_{55} is more significant than 1460 °C. The proportion of this iron ore should not be too high in actual batching. Ore D has a T_R of approximately 3.0 °C. However, the temperature of the region of the sintered layer is usually non-uniform, and a smaller T_R value needs to be avoided as much as possible. The T_R of Ore E is as high as 129 °C, which can adapt well to the high-temperature area with uneven temperature distribution.

3.2. Liquid phase flow index

The liquid-phase flow capacity of iron ore is related to calcium oxide content or the binary alkalinity and the sintering temperature. Fig. 7 shows ore samples' liquid phase flow index with the alkalinity of 2.0, 3.0, and 4.0 sintered at 1300°C and 1320°C. Among them, the Ore C hardly melted obviously within 1350°C, so the experimental measurement of the liquid phase flow index of the Ore C was not carried out.

The liquid-phase flow capacity relationship from the liquid-phase flow index results of different kinds of ores sintered at 1300°C was Mixed Ore > Ore D > Ore A > Ore B \approx Ore E. A top view of the sintered mixed ore with different alkalinity at different

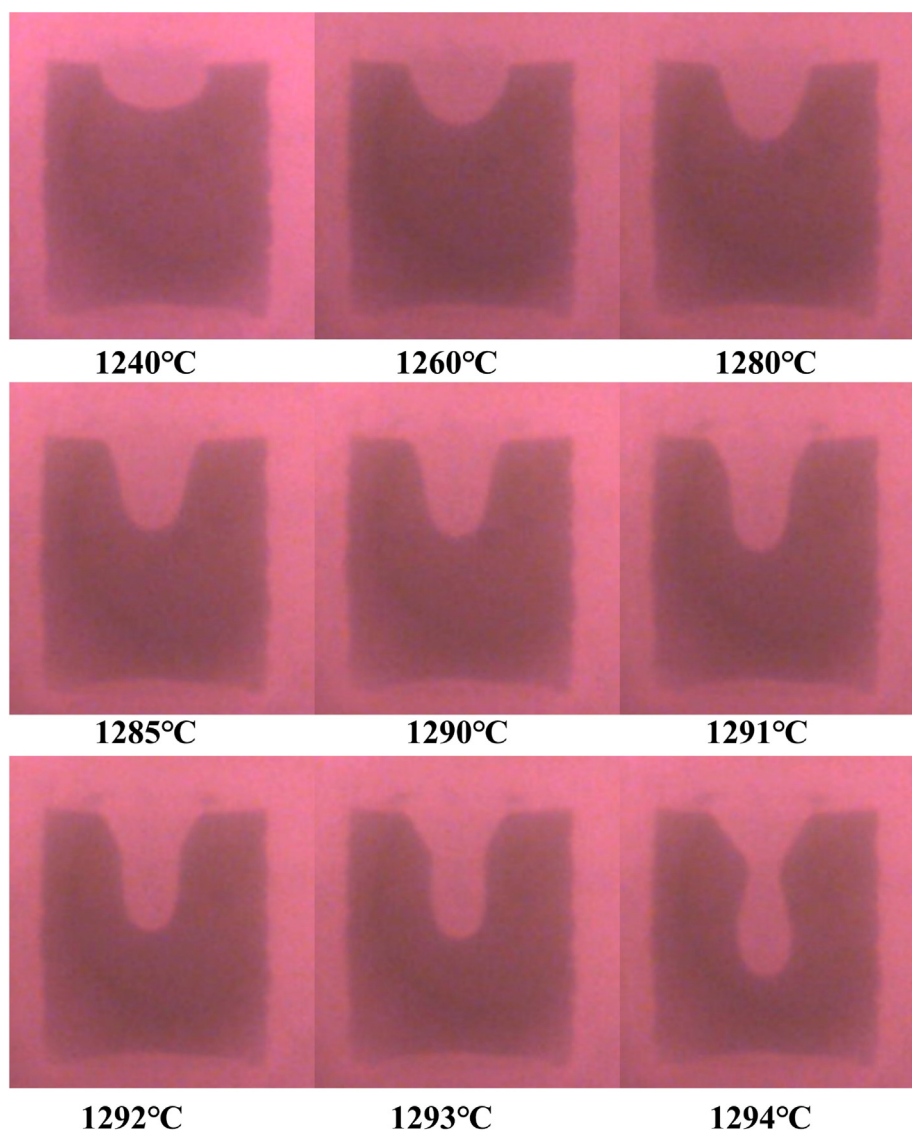


Fig. 9. Schematic diagram of the flow process of mixed iron ore.

sintering temperatures is shown in Fig. 8. In general, the relationship between liquid phase flow index and melt characteristic of the different iron ores is in good agreement. The liquid phase flow index of Ore A, Ore D, and Mixed Ore increased obviously with alkalinity. This was due to the reaction of calcium oxide with iron ore at high temperatures to form calcium and iron oxides, such as calcium ferrite, forming a sizeable liquid phase (Zhou et al., 2020a). The liquid phase flow index of iron Ore B and Ore E was not obviously affected by alkalinity. T_{20} values for Ore B and Ore E with the alkalinity of 4.0 are in Table 5, with T_{20} values around 1320 °C. Thus, it was challenging to generate a liquid phase for Ore B and Ore E with the alkalinity of 4.0 at 1300 °C, not to mention samples with lower alkalinities. At 1320 °C, Ore B and Ore E with the alkalinity of 4.0 produced a lower liquid phase than other ores. Therefore, higher alkalinity than 4.0 or a higher sintering temperature than 1320 °C is required to promote the melting of Ore B and Ore E.

Compared with the ore samples sintered at 1300 °C, the liquid phase flow indexes of the samples sintered at 1320 °C in Fig. 7(b) increased to some extent. The liquid phase flow index increased with increasing alkalinity for almost all ore samples. It is worth noting that the liquid phase flow index of samples with the alkalinity of 3.0–4.0 sintered at 1300 °C did not increase significantly. However, when the sintering temperature increased to 1320 °C, most samples' liquid phase flow index increased considerably, which further indicated that the increase in the sintering temperature could promote the liquid phase flow of the ore.

In summary, the factors that affect ore's liquid phase flow index include the type of ore, sintering temperature, and alkalinity. In the actual sintering process, due to the consideration of the characteristics of the ore itself, the appropriate alkalinity value and fuel can be prepared to obtain high-quality iron ore sinter.

3.3. High-temperature flow characteristic

The iron ore samples gradually formed a liquid phase during the experiment with increasing temperature. The flow process of the mixed iron ore with alkalinity 4.0 is shown in Fig. 9. The flow of the iron ore sample was jointly completed under the action of gravity, surface tension, and other forces. Fig. 10(a-c) shows the variation of flow length and velocity with the temperature for mixed iron ores of different alkalinity. The Ore-2.0 had no apparent flow before 1300 °C, and when the temperature reached 1320 °C, the flow rate of the ore was relatively low. This was in agreement with the experimental results in the previous section, where the liquid phase flow index was small for the sample with alkalinity 2.0. The critical flow temperature T_C was defined as a temperature of a sudden change in flow rate.

The T_C of Ore-2.0 was 1359 °C, which meant that only when the temperature exceeded 1359 °C did the liquid phase fluidity of the sample with this alkalinity increase. When the temperature increased to around 1384 °C, the ore sample formed a melt and dripped, indicating that the liquid phase of the ore had good fluidity. The flow characteristics of Ore-3.0 and Ore-4.0 ore samples

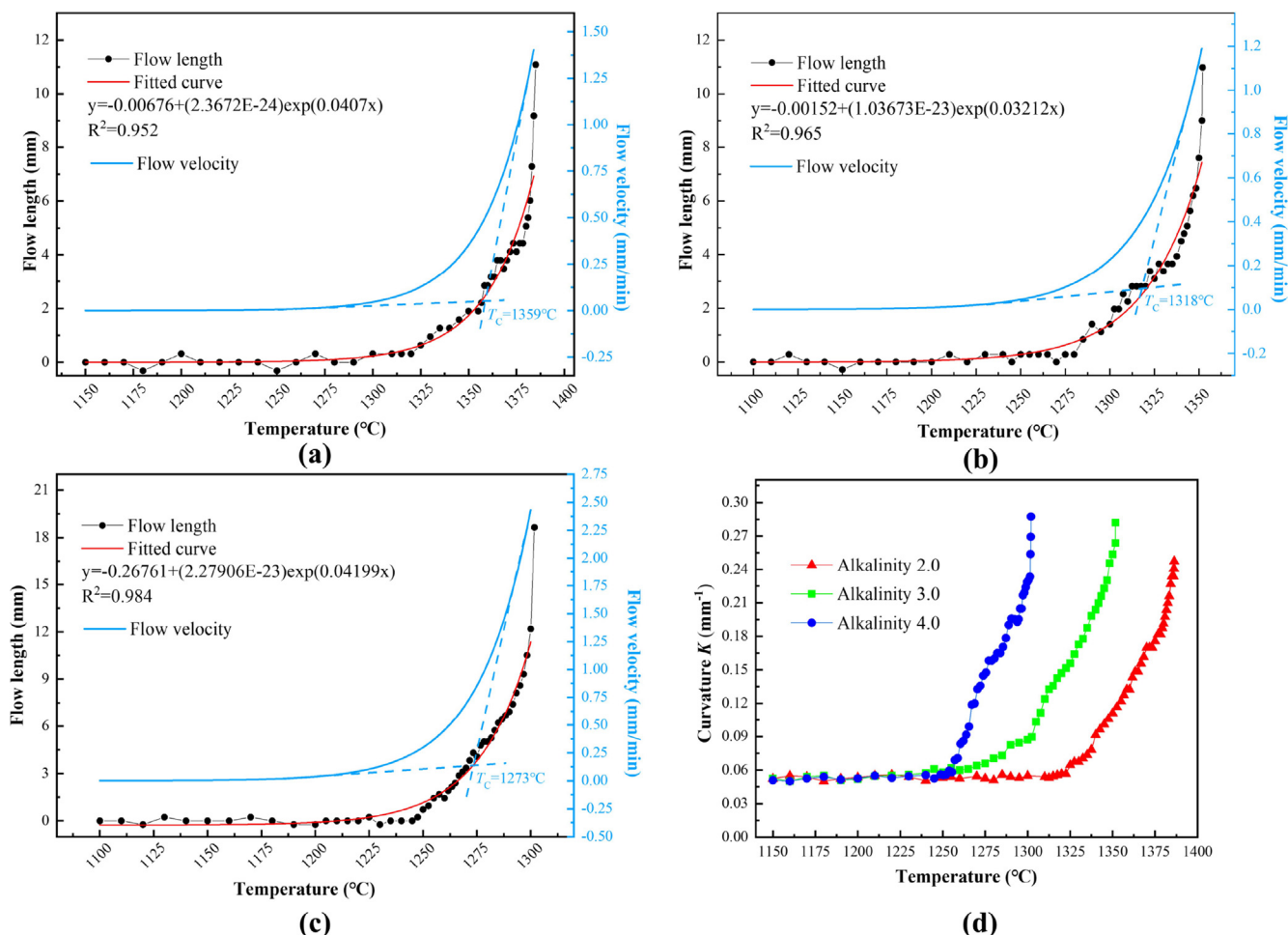


Fig. 10. Flow characteristic of ore samples with alkalinity (a)2.0 (b)3.0 (c)4.0 as a function of temperature; (d)bottom curvature of iron ore samples as a function of temperature.

Table 6
Flow characteristic temperatures of iron ore samples under different alkalinity.

Alkalinity	T_C (°C)	T_T (°C)	T_E (°C)
2.0	1359	1384	25
3.0	1318	1351	33
4.0	1273	1301	28

were similar to Ore-2.0, and the flow temperature decreased with the increase of alkalinity.

The liquid phase fluidity of iron ore needs to be moderate in the practical application to obtain higher quality sinter. To further discuss the flow characteristic of mixed iron ore, T_C was also defined as the effective initial flow temperature of the ore, and the melt dripping temperature T_T was defined as the effective termination flow temperature. The difference between them was defined as the effective flow temperature interval T_E . The three newly defined characteristic parameters corresponded to T_{20} , T_{55} , and T_R . The mobile phase of the ore is minimal before T_C and cannot flow and diffuse effectively to bond more of the sinter mix. In the ore sample, a large amount of melt is generated after T_T , and it is easy to form a sintered layer beyond the melting point, making the permeability of the bed worse. The most suitable sintering temperature should therefore be controlled somewhere in between. Table 6 shows the flow characteristic temperature of each ore. The flow characteristic temperature decreased with the increase of alkalinity. So, increasing alkalinity could improve the fluidity of iron ore. This was consistent with the results of the melt characteristic experimental. According to iron ore's three flow characteristic temperatures and flow velocity curves, iron ore's high-temperature flow characteristic can be more intuitively understood.

As the temperature increased, the resulting liquid phase continued to move towards the bottom of the sample, and the bottom gradually tended to bend under surface tension. Fig. 10(d) shows the change in the bottom curvature of different iron ore samples with temperature. The bottom curvature of iron ore samples under

each working condition increased gradually with increasing temperature.

Ore-2.0 and Ore-4.0 began to bend at about 1310 °C and 1255 °C, indicating that the liquid phase began to be generated at this time. In general, the bottom curvature of the iron ore sample corresponded to the change in its flow velocity. The flow velocity more intuitively reflected the fluidity of the iron ore, and the bottom curvature reflected the bottom melt's shape and size, reflecting the formed melt' quality.

3.4. Evolution of pore structure

The pore structure of the samples sintered at 1300 °C and 1320 °C were 3D reconstructed by XCT, as shown in Fig. 11. The left side of the figure is the reconstructed image of the whole ore sample, and the right side is the internal pore structure diagram of the corresponding sample. All views are in the direction of the top view. The pore structure distribution of Ore-2.0 sintered at 1300 °C was sparse, and the pore structure distribution was denser when the alkalinity increased. Interestingly, the samples sintered at 1320 °C showed the opposite trend. This suggested that the pore structure was related to the binary alkalinity of the ore and the heating conditions. More notably, pores closer to the surface were smaller and relatively sparsely distributed. During the sintering process, the surface temperature was relatively high due to the furnace's heating characteristics, and the liquid phase formed first on the surface. Based on this, according to the latest research by Wang and Zhou et al. (Wang et al., 2021; Zhou et al., 2021a), the pore structure's evolution process of the samples during the sintering process can be roughly divided into the generation stage of pores, the fusion stage between pores and the rupture or overflow stage of pores. The melt and flow of the sample directly affect the break and overflow of pores. It was found that greater melt fluidity facilitates the movement of internal pores and diffusion to the external environment. The pores diffused to the sample's surface would break and overflow, thereby reducing the porosity (Huang et al.,

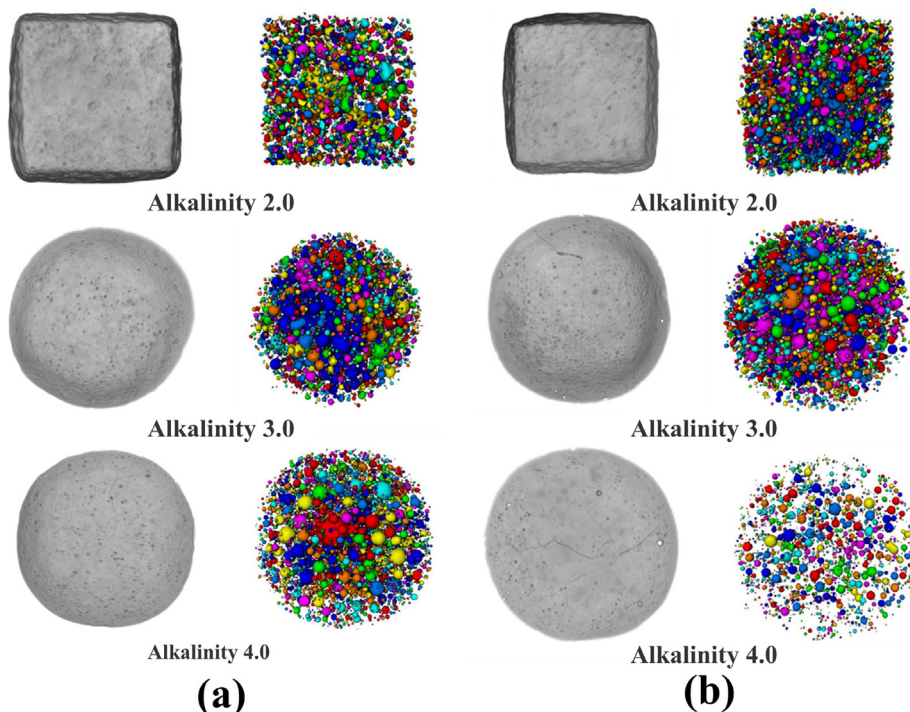


Fig. 11. Reconstruction map of the ore sample and its pore structure after sintering at (a) 1300 °C and (b) 1320 °C.

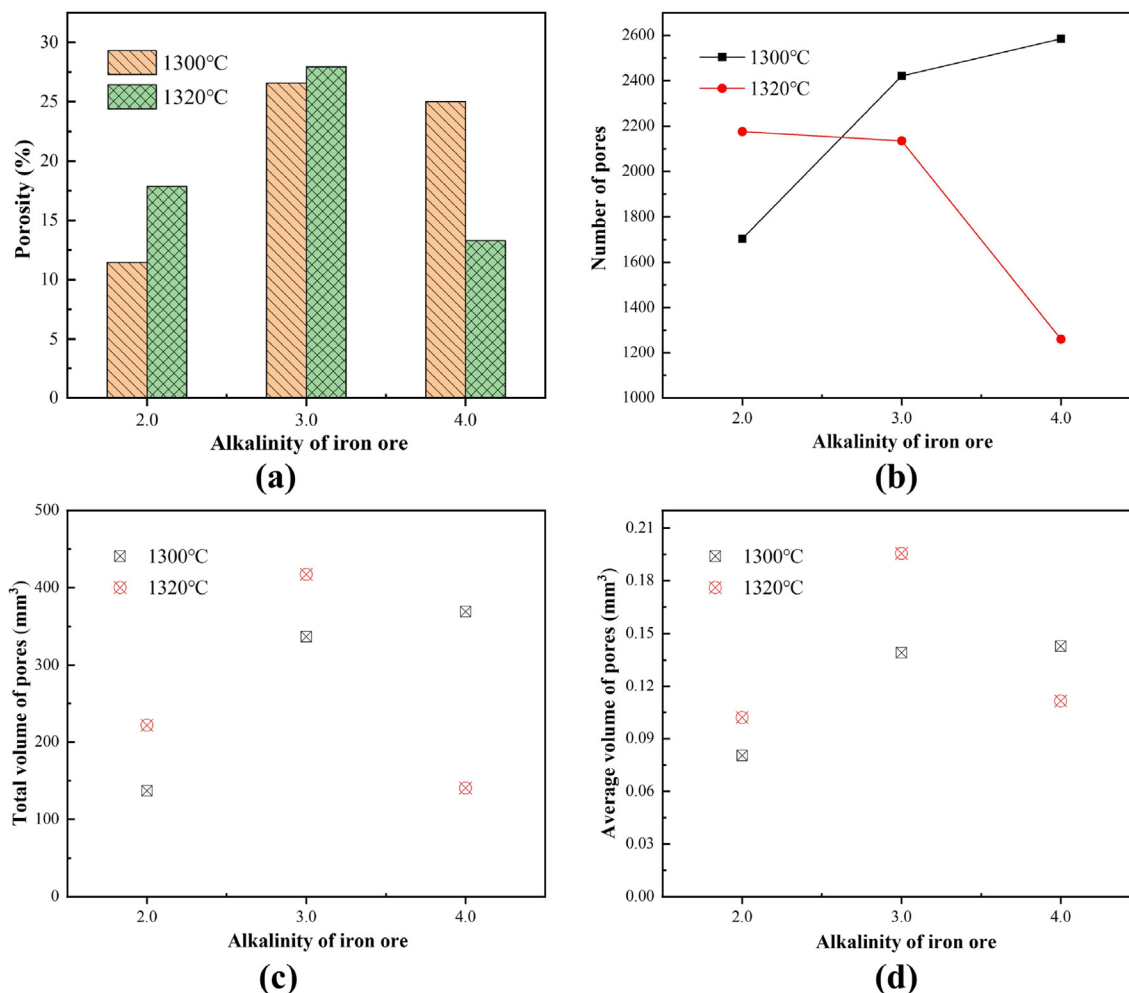


Fig. 12. (a) Overall porosity (b) number of pores (c) total pore volume (d) average pore volume of mixed ores with different alkalinity sintered at 1300 °C and 1320 °C.

2020). Therefore, the change in the fluidity of the sample will significantly influence its pore structure.

Fig. 12(a) shows the overall porosity of mixed iron ores with different alkalinity at different sintering temperatures. The overall porosity of the Ore-2.0 sintered at 1300°C was 11.45 %. While the overall porosity of Ore-3.0 and Ore-4.0 remained at a high level, 26.58 % and 25.02 %, respectively. Combined with the previous iron ore melt and flow characteristic experiments, Ore-2.0 at 1300 °C did not change significantly. Therefore, it could be inferred that very little gas was generated within the sample under this condition. The degree of thermal expansion of the sample was very shallow, and the pore structure was still in the pore generation stage. Increasing the alkalinity can reduce the melting point of the ore. Therefore, the higher the alkalinity of the ore at the same temperature, the more pore structures are produced, and the porosity is higher. The porosity of the Ore-2.0 sintered at 1320 °C increased to 17.87 %. Ores not significantly sintered at 1300 °C were sintered to a greater extent at 1320 °C, and more pore structures were created. However, when the alkalinity of the ore increased, the porosity first increased and then decreased. The Ore-4.0 at 1320°C had good liquid-phase fluidity, promoting the diffusion and overflow of pores in the sample and reducing the porosity.

However, the volume of the sintered sample would change, and the overall porosity could not comprehensively summarize the porosity parameters of the sample. Fig. 12(b-d) shows the number of pores, total pore volume, and the average pore volume of different samples. The average volume of pores is the ratio of the total

volume of pores to the number of pores. The total pore volume of the sample represents the degree of expansion of the ore sample or the amount of gas generated during sintering, and the average pore volume represents the degree of pore fusion. With the continuous pore evolution, the pore structure in the sample first increased and then decreased. At 1300 °C, the parameters such as pore number and pore volume of ore samples increased with alkalinity. Although the porosity of Ore-4.0 was slightly lower, the number of pores and pore volume of Ore-4.0 was raised, which meant that the working condition of Ore-4.0 promoted the formation of pores. The pores of the samples at 1320 °C tended to break and overflow more easily due to the increased alkalinity of the iron ore. Therefore, the number of pores gradually decreased, and the average pore volume first increased and then decreased. This was due to the increased mobility of the liquid phase of the sample.

In the actual sintering process, too low porosity will affect the smelting of the sinter, and too high porosity will affect the strength of the sinter. Therefore, the alkalinity and sintering temperature can be appropriately adjusted to obtain suitable fluidity and porosity.

4. Conclusion

In this work, the melt characteristic and liquid phase flow index of different iron ores were first investigated, and the mixed ore behaved best.

Then, parameters such as flow velocity, characteristic temperature, and bottom curvature were obtained using the method of visual measurement to comprehensively evaluate the flow characteristic of ore. The results showed that the flow velocity of iron ore was exponentially related to temperature. The flow characteristic parameters T_C , T_T , and T_E of iron ore were obtained from the relationship between flow rate and temperature. The T_C of the Ore-2.0, Ore-3.0, and Ore-4.0 were 1359 °C, 1318 °C and 1273 °C, respectively, and T_T were 1384 °C, 1351 °C and 1301 °C, respectively. The bottom curvature of the sample during heating reflected the shape, size, and quality of the bottom melt.

Finally, the related parameters of the pore structure of sintered ore samples were obtained by XCT, and the effect of high-temperature fluidity of iron ore on pore evolution was clarified. The results showed that improving sample fluidity would promote the diffusion and overflow of pores during the sintering process. Increasing the alkalinity of the sintered samples at 1300 °C would promote pore structure development. When the sintering temperature increased, increasing the alkalinity could significantly promote the improvement of fluidity and the decrease of porosity.

CRedit authorship contribution statement

Mengting Ji: Conceptualization, Methodology, Data curation, Writing – original draft. **Jiawei Luo:** Visualization, Investigation. **Hao Zhou:** Resources, Supervision, Writing – review & editing.

Data availability

No data was used for the research described in the article.

Declaration of Competing Interest

The authors declare that they have no known competing financial interests or personal relationships that could have appeared to influence the work reported in this paper.

Acknowledgement

This work was supported by National Natural Science Foundation of China (52036008).

References

- Dong, J.J., Wang, G., Gong, Y.G., Xue, Q.G., Wang, J.S., 2015. Effect of high alumina iron ore of gibbsite type on sintering performance. *Ironmak. Steelmak.* 42, 34–40. <https://doi.org/10.1179/1743281214Y.0000000195>.
- He, C., Ilyushechkin, A., Bai, J., Hla, S.S., Kong, L.-X., Li, W., 2021. Viscosity and crystallisation behaviour of coal ash slag from the primary phase of anorthite. *Fuel Process. Technol.* 213, 106680.
- Huang, Q., Liu, T., Zhang, J., He, X.i., Liu, J., Luo, Z., Lu, A., 2020. Properties and pore-forming mechanism of silica sand tailing-steel slag-coal gangue based permeable ceramics. *Constr. Build. Mater.* 253, 118870.
- Ilic, M., Cheeseman, C., Sollars, C., Knight, J., 2003. Mineralogy and microstructure of sintered lignite coal fly ash. *Fuel* 82, 331–336. [https://doi.org/10.1016/S0016-2361\(02\)00272-7](https://doi.org/10.1016/S0016-2361(02)00272-7).
- Kasai, E., Sakano, Y., Nakamura, T., 2000. Influence of iron ore properties on the flow of melt formed in the sintering process. *Tetsu-To-Hagane/Journal Iron Steel Inst. Japan* 86 (3), 139–145.
- Kou, M.Y., Li, H.P., Wu, S.L., Su, B., Zhang, W.L., 2019. Study on the sintering melting characteristics of Meishan concentrate and its influencing factors. *Ironmak. Steelmak.* 46, 199–205. <https://doi.org/10.1080/03019233.2018.1507069>.
- Liu, X.L., Wu, S.L., Huang, W., Zhang, K.F., Du, K.P., 2014. Influence of high temperature interaction between sinter and lump ores on the formation behavior of primary-slugs in blast furnace. *ISIJ Int.* 54, 2089–2096. <https://doi.org/10.2355/isijinternational.54.2089>.
- Luo, J.W., Zhou, H., Wang, Z.W., Ji, M.T., Meng, H.X., Fang, H., 2021. Experimental study on flow properties of coal ash slag based on the image measurement method. *Asia-Pacific J. Chem. Eng.* 1–13. <https://doi.org/10.1002/apj.2738>.
- Ma, H.Y., Zhao, Z.X., Xin, Y., Ou, S.H., Pan, W., 2020. Evaluation of the Liquid Phase Fluidity During Iron Ore Sintering. *Minerals, Metals and Materials Series.*

- Springer International Publishing. https://doi.org/10.1007/978-3-030-36540-0_55.
- Ni, W.J., Li, H.F., Shao, L., Zou, Z.S., 2020. Numerical simulation on influence of coke oven gas injection on iron ore sintering. *ISIJ Int.* 60, 662–673. <https://doi.org/10.2355/isijinternational.ISIJINT-2019-533>.
- Peng, J., Zhang, L., Liu, L.X., An, S.L., 2017. Relationship Between Liquid Fluidity of Iron Ore and Generated Liquid Content During Sintering. *Metall. Mater. Trans. B Process Metall. Mater. Process. Sci.* 48, 538–544. <https://doi.org/10.1007/s11663-016-0827-2>.
- Shatkhva, V., Korobeynikov, I., Maire, E., Grémillard, L., Adrien, J., 2010. Iron ore sinter porosity characterisation with application of 3D X-ray tomography. *Ironmak. Steelmak.* 37, 313–319. <https://doi.org/10.1179/030192310X12683045805865>.
- Wang, W., Chen, X.H., Xu, R.S., Li, J., Shen, W.J., Wang, S.P., 2020. Research progress on multiscale structural characteristics and characterization methods of iron ore sinter. *J. Iron Steel Res. Int.* 27, 367–379. <https://doi.org/10.1007/s42243-020-00374-4>.
- Wang, Z.W., Zhou, H., Li, Y., Zhang, P.C., Mao, R., Ren, L.M., Luo, J.W., 2021. Experimental Study of the Pore Structure during Coal and Biomass Ash Sintering Based on X-ray CT Technology. *Energy and Fuels* 35, 2098–2109. <https://doi.org/10.1021/acs.energyfuels.0c03668>.
- Wu, S., Zhai, X., 2018. Factors influencing melt fluidity of iron ore. *Metall. Res. Technol.* 115 (5), 505.
- Wu, S., Zhang, G., Chen, S., Su, B., 2014. Influencing factors and effects of assimilation characteristic of iron ores in sintering process. *ISIJ Int.* 54, 582–588. <https://doi.org/10.2355/isijinternational.54.582>.
- Wu, S., Su, B., Qi, Y., Kou, M., Li, Y., Zhang, W., 2017. Melt Absorbability of Iron Ore Nuclei and Its Influence on Suitable Liquid Content of Sintered Body. *Metall. Mater. Trans. B Process Metall. Mater. Process. Sci.* 48, 2469–2480. <https://doi.org/10.1007/s11663-017-1059-9>.
- Wu, S., Li, H., Zhang, W., Su, B.o., 2019. Effect of thermodynamic melt formation characteristics on liquid phase fluidity of iron ore in the sintering process. *Metals (Basel)*. 9 (4), 404.
- Xiao, Z.X., Chen, L.K., Yang, Y.D., Li, X.C., Barati, M., 2017. Effect of coarse-grain & low-grade iron ores on sinter properties. *ISIJ Int.* 57, 795–804. <https://doi.org/10.2355/isijinternational.ISIJINT-2016-688>.
- Yang, C., Yang, C., Li, J., Li, Y., Yan, F., 2022. Forecasting of iron ore sintering quality index: A latent variable method with deep inner structure. *Comput. Ind.* 141, <https://doi.org/10.1016/j.compind.2022.103713>.
- Zhai, X.B., Wu, S.L., Zhou, H., Su, L.X., Ma, X.D., 2020. Flow and penetration behaviours of liquid phase on iron ore substrate and their effects on bonding strength of sinter. *Ironmak. Steelmak.* 47, 405–416. <https://doi.org/10.1080/03019233.2018.1537223>.
- Zhang, X., He, S.Y., Sun, H.Y., Zhu, Q.S., Li, J., Li, H.Z., 2020. Mechanism of surface morphology evolution in the reduction of fine iron ore in a conical fluidized bed reactor. *Chem. Eng. Sci.* 220, <https://doi.org/10.1016/j.ces.2019.115468>.
- Zhang, J.L., Hu, Z.W., Zuo, H.B., Liu, Z.J., Yang, T.J., Zhao, Z.X., 2014b. Ore blending ratio optimisation for sintering based on iron ore properties and cost. *Ironmak. Steelmak.* 41, 279–285. <https://doi.org/10.1179/1743281213Y.0000000134>.
- Zhang, H.X., Xian, S.X., Fan, Y.Q., Dong, P.F., Zhu, Z.P., 2021. A perspective on sodium-induced agglomeration of Zhundong coal gasification: Experiments and calculations. *J. Energy Inst.* 94, 39–48. <https://doi.org/10.1016/j.joei.2020.10.006>.
- Zhou, M., Jiang, T., Yang, S.T., Xue, X.X., 2015b. Vanadium-titanium magnetite ore blend optimization for sinter strength based on iron ore basic sintering characteristics. *Int. J. Miner. Process.* 142, 125–133. <https://doi.org/10.1016/j.minpro.2015.04.019>.
- Zhou, H., Liu, Z.H., Cheng, M., Zhou, M.X., Liu, R.P., 2015a. Influence of coke combustion on NOx emission during iron ore sintering. *Energy and Fuels* 29, 974–984. <https://doi.org/10.1021/ef502524y>.
- Zhou, H., Zhou, M.X., Cheng, M., Guo, W.S., Cen, K.F., 2017. Experimental study and X-ray microtomography based CFD simulation for the characterization of pressure drop in sinter bed. *Appl. Therm. Eng.* 112, 811–819. <https://doi.org/10.1016/j.applthermaleng.2016.10.123>.
- Zhou, H., Zhou, M.X., Ma, P.N., Cheng, M., 2019. Experimental investigation on the flame front resistance of gas channel growth with melt formation in iron ore sinter beds. *Proc. Combust. Inst.* 37, 4607–4615. <https://doi.org/10.1016/j.proci.2018.09.027>.
- Zhou, H., Ma, P., Lai, Z., Zuo, Y., Xing, Y., Shi, H., Cen, K., 2020a. Harmless treatment of waste selective catalytic reduction catalysts during iron ore sintering process. *J. Clean. Prod.* 275, 122954.
- Zhou, H., Luo, J., Wang, Z., Ji, M., Zhang, M., 2021a. Effect of walnut shell ash on pore structure characteristics during Zhundong coal sintering. *Fuel Process. Technol.* 221, 106923.
- Zhou, H., Wang, J.K., Ma, P.N., Meng, H.X., Cheng, F.Z., Luo, J.W., 2021b. Influence of quick lime on pore characteristics of high-temperature zone in iron ore sinter based on XCT technology. *J. Mater. Res. Technol.* 15, 4475–4486. <https://doi.org/10.1016/j.jmrt.2021.10.061>.
- Zhou, H., Meng, H.X., Ma, P.N., Wang, J.K., 2022. Effect of coke ratio on pore structure evolution in the high-temperature zone of sintering bed. *J. Energy Inst.* 100, 189–196. <https://doi.org/10.1016/j.joei.2021.11.014>.
- Zhou, M.X., Xu, J.N., Zhou, H., 2020b. Evaluating the permeability properties of green bed in iron ore sintering using high resolution X-ray computed tomography and orthogonal array tests. *Powder Technol.* 375, 360–368. <https://doi.org/10.1016/j.powtec.2020.08.007>.